Proceedings of the Sixteenth International Conference on
Computational Structures Technology
Edited by: P. Iványi, J. Kruis and B.H.V. Topping
Civil-Comp Conferences, Volume 14, Paper 6.1
Civil-Comp Press, Edinburgh, United Kingdom, 2026
ISSN: 2753-3239, doi: 10.4203/ccc.14.6.1

Topology Optimisation of Lattice Structures for Strain-Tunable Wave Filtering

F. Gomez Silva[1], R. Ortigosa[2] and J. Martinez-Frutos[2]

[1] University Carlos III of Madrid, Spain
[2] Technical University of Cartagena, Spain

Abstract

Excessive vibrations in engineering systems can compromise performance, fatigue life and comfort, and may also lead to noise amplification, loss of precision in sensitive components, and increased maintenance requirements. These challenges motivate the development of adaptive wave-filtering materials. This work presents a topology optimization algorithm for bi-material lattice structures with a band gap at a target frequency, using a single unit cell via the Bloch-Floquet theorem. The BESO method with bi-material interpolation is employed, along with a new objective function that considers only the natural frequencies nearest the target, reducing computational cost and improving robustness as these frequencies adapt to material distribution. A novel approach is also introduced to determine the optimal material volume fraction, allowing the algorithm to autonomously maximize the band gap. The method is tested on 1D-CR and 2D-CR lattice structures, with selected results compared to existing approaches.

Keywords: 2D lattice structures, band gaps, BESO optimization algorithm, bi-material interpolation, topology optimization, metamaterial

1 Introduction

The design of lattice structures with tailored dynamic properties has attracted significant attention in recent years, particularly in the context of wave propagation control, vibration isolation, and frequency filtering. Such structures, often composed of repeating unit cells, allow for the formation of band gaps—frequency ranges in which wave propagation is suppressed—making them highly suitable for applications in acoustics, mechanics, and metamaterials. Traditional approaches to lattice optimization rely on selecting the volume fraction of constituent materials a priori, followed by iterative adjustments of their spatial distribution to achieve the desired mechanical or dynamic performance. However, this strategy requires multiple trial-and-error runs, which can be computationally demanding and may not guarantee the identification of the optimal material configuration.

Topology optimization techniques provide a systematic framework to address this challenge, and among them, the Bi-directional Evolutionary Structural Optimization (BESO) method has emerged as a widely adopted and robust approach. BESO offers a discrete, gradient-based procedure in which the sensitivity of the objective function with respect to each finite element is evaluated, and the material distribution is iteratively updated. Despite its effectiveness, most existing BESO implementations treat the final volume fraction as an input parameter, limiting the ability to simultaneously optimize both the topology and the material fraction. Moreover, issues such as mesh dependency and checkerboard patterns may compromise the quality of the obtained designs, necessitating the use of numerical filters to ensure smooth and physically meaningful topologies.

This work proposes a novel extension of the BESO algorithm in which the volume fraction of material 1 is treated as an output variable. The proposed procedure allows the algorithm to determine not only the optimal topology but also the optimal volume fraction that maximizes a user-defined objective function, providing a more efficient and automated approach to lattice optimization. A slope-based detection strategy is introduced to identify the optimal fraction during the evolution process, while convergence is assessed using a historical average-based stopping criterion. Numerical filters are applied to suppress numerical instabilities and enforce a minimum feature size. The methodology is validated through several numerical examples involving one-dimensional and two-dimensional periodic lattice structures, demonstrating the effectiveness of the approach in achieving band gaps around target frequencies while reducing computational cost compared to conventional methods.

The contributions of this work are threefold: (i) the simultaneous optimization of both topology and volume fraction within a BESO framework, (ii) the introduction of a robust detection procedure for the optimal volume fraction, and (iii) the application and validation of the methodology for frequency-targeted lattice design in both 1D and 2D configurations. The results confirm that the proposed method provides reliable, reproducible designs with enhanced dynamic performance, paving the way for more efficient lattice-based metamaterial structures.

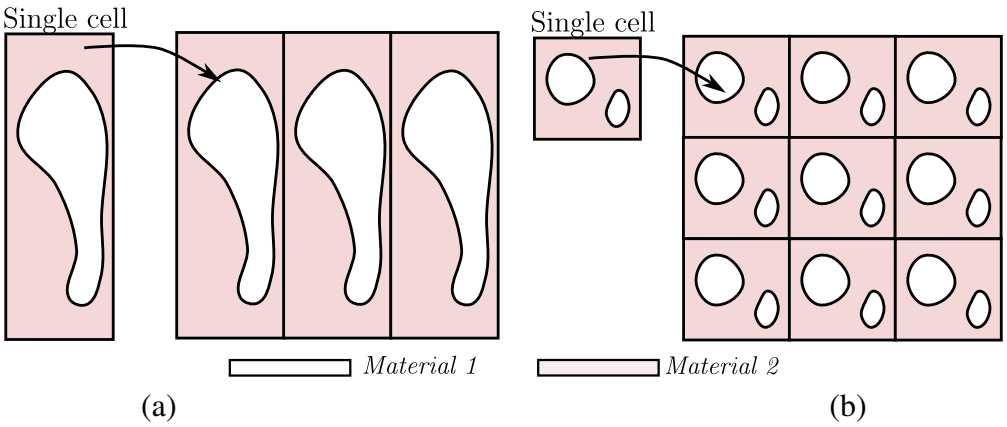

Figure 1: Illustration of the concept of: (a) 1D-CR lattice structures; (b) 2D-CR lattice structures. Finite repetition of a single unit cell in both types of lattice structures considered in this work.

2 Eigenvalue optimization problem statement

This study addresses the topology optimization of two-dimensional lattice structures composed of two distinct materials and governed by linear elastic behavior. The lattices are designed to undergo in-plane displacements and are generated through the periodic repetition of a single unit cell. Depending on the repetition pattern, two configurations are considered: repetition along a single spatial direction and repetition along two spatial directions. These cases are denoted throughout this manuscript as *one-dimensional cell repetition* (1D-CR) and *two-dimensional cell repetition* (2D-CR), respectively. A graphical representation of both lattice configurations is provided in Figure 1.

The primary goal of the optimization process is to identify an optimal spatial arrangement of the two materials such that the resulting lattice exhibits dispersion characteristics featuring frequency intervals of inhibited wave propagation, commonly referred to as *band gaps*, in the vicinity of a prescribed target frequency ω_0. A schematic explanation of the band-gap concept is shown in Figure 5. Within these frequency intervals, mechanical waves generated at an excitation point are unable to propagate through the optimized lattice.

Bloch's theorem plays a central role in this framework, as it enables the dynamic response of the infinite periodic structure to be characterized through the analysis of a single representative unit cell. To this end, a finite element discretization is introduced on the unit cell domain, where both constituent materials are distributed in accordance with the optimization variables so as to enhance the lattice's wave attenuation performance. Each finite element is associated with a discrete design variable x_i, which takes the value $x_i = 1$ if the element is occupied by material 1 and $x_i = 0$ if it is assigned material 2, as illustrated in Figure 2.

Prior to describing the topology optimization strategy in detail, the formulation of

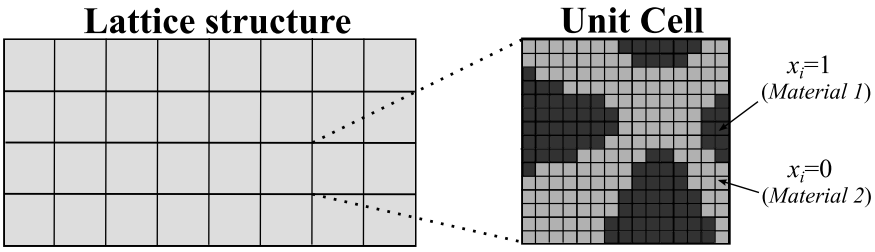

Figure 2: Schematic representation of the optimization procedure based on Bloch's theorem.

the free-vibration eigenvalue problem is introduced, together with the application of Bloch's theorem to periodic lattice structures.

2.1 Fundamentals on wave propagation

Let Ω denote the two-dimensional lattice structure depicted in Figure 2, composed of a collection of periodically arranged unit cells. The periodicity of the lattice is defined by the vectors $\mathbf{e}_1 = \ell_x \mathbf{i}$ and $\mathbf{e}_2 = \ell_y \mathbf{j}$, where ℓ_x and ℓ_y represent the unit-cell dimensions along the x- and y-directions, respectively (see Figure 3). The propagation of elastic waves within the domain Ω is governed by the linear elastodynamic equation

$$\boldsymbol{\nabla} \cdot \boldsymbol{\sigma}(\boldsymbol{\varepsilon}(\mathbf{u})) = \rho \frac{\partial^2 \mathbf{u}}{\partial t^2} \qquad \text{in } \Omega. \tag{1}$$

In Eq. (1), ρ denotes the material density, $\boldsymbol{\sigma}$ is the Cauchy stress tensor, and $\boldsymbol{\varepsilon}(\mathbf{u})$ corresponds to the infinitesimal strain tensor associated with the displacement field $\mathbf{u}$. The strain tensor is defined as the symmetric part of the displacement gradient,

$$\boldsymbol{\varepsilon}(\mathbf{u}) = \frac{1}{2}\left(\boldsymbol{\nabla}\mathbf{u} + \boldsymbol{\nabla}\mathbf{u}^T\right). \tag{2}$$

For isotropic linear elastic materials, the stress–strain relationship is given by

$$\boldsymbol{\sigma}(\boldsymbol{\varepsilon}(\mathbf{u})) = 2\mu\boldsymbol{\varepsilon}(\mathbf{u}) + \lambda\,\mathrm{tr}(\boldsymbol{\varepsilon}(\mathbf{u}))\,\boldsymbol{I}, \tag{3}$$

where $\boldsymbol{I}$ is the second-order identity tensor, and μ and λ are the Lamé parameters. As is well established in the literature [2, 3], the dispersion characteristics of a linear elastic medium can be obtained by seeking solutions of Eq. (1) in the form of harmonic plane waves. Accordingly, the displacement field is assumed as

$$\mathbf{u}(\mathbf{r}, t) = \mathcal{U}(\mathbf{r}, t) = \mathbf{U}_0\, e^{\,i(\boldsymbol{\kappa}\cdot\mathbf{r} - \omega t)} = \mathbf{U}(\mathbf{r})\, e^{-i\omega t}, \tag{4}$$

where $\boldsymbol{\kappa}$ is the wave vector, ω is the angular frequency, and $\mathbf{r}$ denotes the position vector. The spatial dependence of the solution is contained in the mode shape $\mathbf{U}(\mathbf{r})$, while the exponential terms describe the oscillatory behavior in space and time.

Substituting the ansatz (4) into the governing elastodynamic equation (1) leads to the following eigenvalue problem for the mode shapes:

$$\boldsymbol{\nabla} \cdot \boldsymbol{\sigma}(\boldsymbol{\varepsilon}(\mathbf{U})) = \rho\,\omega^2 \mathbf{U} \qquad \text{in } \Omega. \tag{5}$$

2.2 Wave propagation in periodic media: Bloch-Floquet theorem

The *Bloch theorem* [1] constitutes a fundamental framework for the analysis of wave propagation in periodic lattice media. By exploiting the translational symmetry inherent to such systems, the theorem allows the dispersion properties of an infinite lattice to be determined through the study of a single representative unit cell. In this context, the displacement mode shapes $\mathbf{U}(\mathbf{r})$ are expressed as

$$\mathbf{U}(\mathbf{r}) = \mathbf{U}_P(\mathbf{r})\, e^{i\boldsymbol{\kappa}\cdot\mathbf{r}}, \tag{6}$$

where $\mathbf{U}_P(\mathbf{r})$ denotes a periodic function over the lattice. This periodicity is characterized by

$$\mathbf{U}_P(\mathbf{r}+\mathbf{a}) = \mathbf{U}_P(\mathbf{r}), \tag{7}$$

with $\mathbf{a}$ being a lattice translation vector of the form $\mathbf{a} = n\mathbf{e}_1 + m\mathbf{e}_2$, where $n, m \in \mathbb{Z}$. Combining Eqs. (6) and (7) yields the classical Bloch–Floquet relation, which links the mode shapes at spatially translated points,

$$\mathbf{U}(\mathbf{r}+\mathbf{a}) = \mathbf{U}(\mathbf{r})\, e^{i\boldsymbol{\kappa}\cdot\mathbf{a}}. \tag{8}$$

This relation provides a direct means of connecting the displacement fields at equivalent locations in different unit cells. For example, considering the configuration illustrated in Figure 3, let P be a point with coordinates $\mathbf{r}^P_{n,m}$ in the unit cell indexed by (n, m), with $n = 1$ and $m = 2$. Since the translation vector satisfies $\mathbf{a} = \mathbf{r}^P_{n,m} - \mathbf{r}^P_{0,0} = n\mathbf{e}_1 + m\mathbf{e}_2$, Eq. (8) leads to

$$\mathbf{U}(\mathbf{r}^P_{n,m}) = \mathbf{U}(\mathbf{r}^P_{0,0})\, e^{i\boldsymbol{\kappa}\cdot\mathbf{a}} = \mathbf{U}(\mathbf{r}^P_{0,0})\, e^{i(n\kappa_x + m\kappa_y)}, \tag{9}$$

where $\kappa_x = \boldsymbol{\kappa}\cdot\mathbf{e}_1$ and $\kappa_y = \boldsymbol{\kappa}\cdot\mathbf{e}_2$ are the components of the wave vector along the primitive lattice directions. This expression relates the displacement at point $P^{(n,m)}$ to that of its corresponding counterpart $P^{(0,0)}$ in the reference unit cell, as depicted in Figure 3.

The Bloch–Floquet condition in Eq. (8) forms the basis for reducing the elastodynamic problem in the extended lattice domain to an equivalent formulation posed on a single unit cell Ω_L. This reduction is achieved by enforcing suitable phase-shift relations between displacement fields at corresponding locations on the boundary $\partial\Omega_L$. For a two-dimensional unit cell, the boundary can be partitioned into distinct regions according to the location of the nodes,

$$\begin{cases} Q_{LB} & \text{bottom-left corner}, & Q_{LT} & \text{top-left corner}, \\ Q_{RB} & \text{bottom-right corner}, & Q_{RT} & \text{top-right corner}, \\ Q_L & \text{left edge (excluding corners)}, & Q_R & \text{right edge (excluding corners)}, \\ Q_B & \text{bottom edge (excluding corners)}, & Q_T & \text{top edge (excluding corners)}. \end{cases} \tag{10}$$

As an illustrative example, consider a point located on the right boundary Q_R and its corresponding point on the opposite boundary Q_L. These points are separated

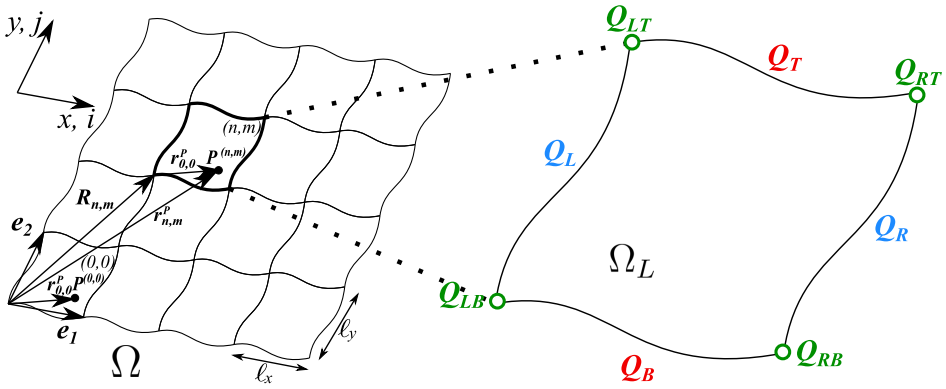

Figure 3: Schematic representation of a discretized two-dimensional unit cell with 2D cell repetition. Finite element nodes are classified according to their location: interior nodes (Q_I), edge nodes (Q_B, Q_R, Q_T, Q_L), and corner nodes (Q_{RB}, Q_{RT}, Q_{LT}, Q_{LB}).

by the translation vector $\mathbf{a} = \mathbf{e}_1$, corresponding to the choice $n = 1$ and $m = 0$. Application of Eq. (8) yields

$$\mathbf{U}_R(\mathbf{r}_L + \mathbf{e}_1) = \mathbf{U}_L(\mathbf{r}_L)\, e^{i\boldsymbol{\kappa}\cdot\mathbf{e}_1} = \mathbf{U}_L(\mathbf{r}_L)\, e^{i\kappa_x}. \tag{11}$$

By selecting appropriate translation vectors for each pair of corresponding boundary regions, the standard Bloch–Floquet periodic boundary conditions for a two-dimensional lattice are obtained:

$$\begin{aligned} \mathbf{U}_R = \mathbf{U}_L e^{i\kappa_x}, \qquad \mathbf{U}_T = \mathbf{U}_B e^{i\kappa_y}, \qquad \mathbf{U}_{RB} = \mathbf{U}_{LB} e^{i\kappa_x}, \\ \mathbf{U}_{LT} = \mathbf{U}_{LB} e^{i\kappa_y}, \qquad \mathbf{U}_{RT} = \mathbf{U}_{LB} e^{i(\kappa_x+\kappa_y)}. \end{aligned} \tag{12}$$

Consequently, the elastic wave propagation problem posed at the lattice level can be reformulated on the unit-cell domain Ω_L as

$$\begin{aligned} \boldsymbol{\nabla}\cdot\boldsymbol{\sigma}(\boldsymbol{\varepsilon}(\mathbf{U})) = \rho\omega^2\mathbf{U} \quad \text{in } \Omega_L, \\ \mathbf{U} \text{ satisfying Eq. (12).} \end{aligned} \tag{13}$$

Following standard finite element procedures, the weak formulation of Eq. (13) is obtained by multiplying by admissible test functions $\mathbf{V}$ and integrating over Ω_L. After application of integration by parts and the divergence theorem, the resulting variational eigenvalue problem reads

$$\int_{\Omega_L} \boldsymbol{\varepsilon}(\mathbf{V}^\dagger) : \boldsymbol{\sigma}(\boldsymbol{\varepsilon}(\mathbf{U}))\, d\Omega_L = \omega^2 \int_{\Omega_L} \rho\, \mathbf{V}^\dagger \cdot \mathbf{U}\, d\Omega_L, \qquad \forall \mathbf{U}, \mathbf{V} \in \mathcal{V}, \tag{14}$$

where $\mathcal{V}$ denotes the space of sufficiently regular functions that satisfy the Bloch–Floquet boundary conditions, and $(\bullet)^\dagger$ indicates complex conjugation.

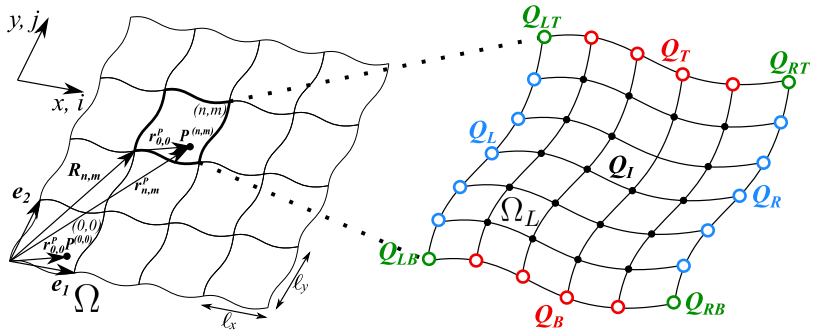

Figure 4: Finite element discretization of two-dimensional unit cell with 2D cell repetition. Nodes are classified according to their position as interior nodes (Q_I), edge nodes (Q_B, Q_R, Q_T, Q_L), and corner nodes (Q_{RB}, Q_{RT}, Q_{LT}, Q_{LB}).

2.3 The discretized eigenvalue problem

The purpose of this section is to derive the spatially discretized formulation of the weak problem introduced in Eq. (14), which governs elastic wave propagation within a single lattice cell Ω_L. This is achieved by applying a standard finite element discretization to the variational statement. The resulting algebraic form reads

$$\boldsymbol{v}^\dagger \cdot \big(\boldsymbol{K} - \omega^2 \boldsymbol{M}\big)\boldsymbol{u} = 0, \tag{15}$$

where $\boldsymbol{K}$ and $\boldsymbol{M}$ denote the stiffness and mass matrices obtained from the discretization of the bilinear forms appearing on the left- and right-hand sides of Eq. (14), respectively. The vectors $\boldsymbol{u}$ and $\boldsymbol{v}$ collect the nodal degrees of freedom associated with the displacement field $\mathbf{U}$ and the test function $\mathbf{V}$.

In addition to Eq. (15), the Bloch–Floquet relations introduced in Eq. (12) must be enforced at the discrete level. To this end, Figure 4, which represents the finite element discretization of the unit cell depicted in Figure 3, is employed. Based on the nodal location within the mesh, the displacement vector can be decomposed as

$$\boldsymbol{u} = \big[u_L,\, u_B,\, u_R,\, u_T,\, u_{LB},\, u_{RB},\, u_{LT},\, u_{RT},\, u_I\big]^T, \tag{16}$$

where the subscripts identify nodal sets located on the boundary $\partial\Omega_L$—consistent with the notation introduced in Eq. (10)—and u_I collects the degrees of freedom associated with interior nodes.

The boundary degrees of freedom are required to satisfy the discrete Bloch–Floquet conditions, namely

$$\begin{aligned} u_R &= u_L e^{i\kappa_x}, \qquad u_T = u_B e^{i\kappa_y}, \qquad u_{RB} = u_{LB} e^{i\kappa_x}, \\ u_{LT} &= u_{LB} e^{i\kappa_y}, \qquad u_{RT} = u_{LB} e^{i(\kappa_x+\kappa_y)}. \end{aligned} \tag{17}$$

Combining Eqs. (15) and (17), the discrete eigenvalue problem can be expressed as

$$\boldsymbol{v}^\dagger \cdot \big(\boldsymbol{K} - \omega^2 \boldsymbol{M}\big)\boldsymbol{u} = 0, \qquad \forall \boldsymbol{u}, \boldsymbol{v} \in \mathcal{V}^h, \tag{18}$$

where $\mathcal{V}^h$ denotes the finite-dimensional space of nodal displacement vectors satisfying the decomposition given in Eq. (16).

Several strategies may be adopted to impose the Bloch–Floquet constraints in Eq. (17). In this work, the conditions are enforced strongly by introducing a reduced set of nodal variables $\widetilde{\boldsymbol{u}}$ through the linear transformation

$$\boldsymbol{u} = \boldsymbol{W}\widetilde{\boldsymbol{u}}, \tag{19}$$

where the transformation matrix $\boldsymbol{W}$ and the reduced displacement vector $\widetilde{\boldsymbol{u}}$ are defined as

$$\boldsymbol{W} = \begin{bmatrix} \boldsymbol{I}_L & 0 & 0 & 0 \\ \boldsymbol{I}_L e^{i\kappa_x} & 0 & 0 & 0 \\ 0 & \boldsymbol{I}_B & 0 & 0 \\ 0 & \boldsymbol{I}_B e^{i\kappa_y} & 0 & 0 \\ 0 & 0 & 1 & 0 \\ 0 & 0 & e^{i\kappa_x} & 0 \\ 0 & 0 & e^{i\kappa_y} & 0 \\ 0 & 0 & e^{i(\kappa_x+\kappa_y)} & 0 \\ 0 & 0 & 0 & \boldsymbol{I}_I \end{bmatrix}, \qquad \widetilde{\boldsymbol{u}} = \begin{bmatrix} u_L \\ u_B \\ u_{LB} \\ u_I \end{bmatrix}. \tag{20}$$

Here, $\boldsymbol{I}_L$, $\boldsymbol{I}_B$, and $\boldsymbol{I}_I$ denote identity matrices whose dimensions correspond to the number of degrees of freedom associated with the node sets Q_L, Q_B, and Q_I, respectively. For the Bloch formulation to be applicable, opposite edges of the unit cell must contain the same number of nodes, positioned at identical coordinates along the periodic directions. Furthermore, corner nodes are linked to the reference corner Q_{LB} to prevent overconstraining the system. In the case of one-dimensional cell repetition (1D-CR), this construction simplifies, and only the condition $u_R = u_L e^{i\kappa_x}$ is required.

Noting that $\boldsymbol{v}^\dagger = (\boldsymbol{W}\widetilde{\boldsymbol{v}})^\dagger = \boldsymbol{W}^\dagger\widetilde{\boldsymbol{v}}^\dagger$, Eq. (18) can be recast as

$$\boldsymbol{W}^\dagger\widetilde{\boldsymbol{v}}^\dagger \cdot \big(\boldsymbol{K} - \omega^2\boldsymbol{M}\big)\boldsymbol{W}\widetilde{\boldsymbol{u}} = 0, \qquad \forall\widetilde{\boldsymbol{v}}. \tag{21}$$

Since this relation must hold for arbitrary $\widetilde{\boldsymbol{v}}$, the following reduced eigenvalue problem is obtained:

$$\big(\boldsymbol{K}_r(\boldsymbol{\kappa}) - \lambda_j\boldsymbol{M}_r(\boldsymbol{\kappa})\big)\widetilde{\boldsymbol{u}}_j = \boldsymbol{0}, \qquad \lambda_j = \omega_j^2, \tag{22}$$

where the reduced stiffness and mass matrices are defined as $\boldsymbol{K}_r = \boldsymbol{W}^H\boldsymbol{K}\boldsymbol{W}$ and $\boldsymbol{M}_r = \boldsymbol{W}^H\boldsymbol{M}\boldsymbol{W}$, with $(\cdot)^H$ denoting the Hermitian transpose. The jth eigenpair $(\lambda_j, \widetilde{\boldsymbol{u}}_j)$ corresponds to the natural frequency ω_j and its associated mode shape.

Since the optimization strategy developed in subsequent sections is formulated in terms of natural frequencies, it is convenient to isolate the eigenvalues explicitly. Premultiplying Eq. (22) by $\widetilde{\boldsymbol{u}}_j^T$ leads to the Rayleigh quotient

$$\lambda_j = \omega_j^2 = \frac{\widetilde{\boldsymbol{u}}_j^T\boldsymbol{K}_r\widetilde{\boldsymbol{u}}_j}{\widetilde{\boldsymbol{u}}_j^T\boldsymbol{M}_r\widetilde{\boldsymbol{u}}_j} = \frac{\boldsymbol{u}_j^T\boldsymbol{K}\boldsymbol{u}_j}{\boldsymbol{u}_j^T\boldsymbol{M}\boldsymbol{u}_j}, \tag{23}$$

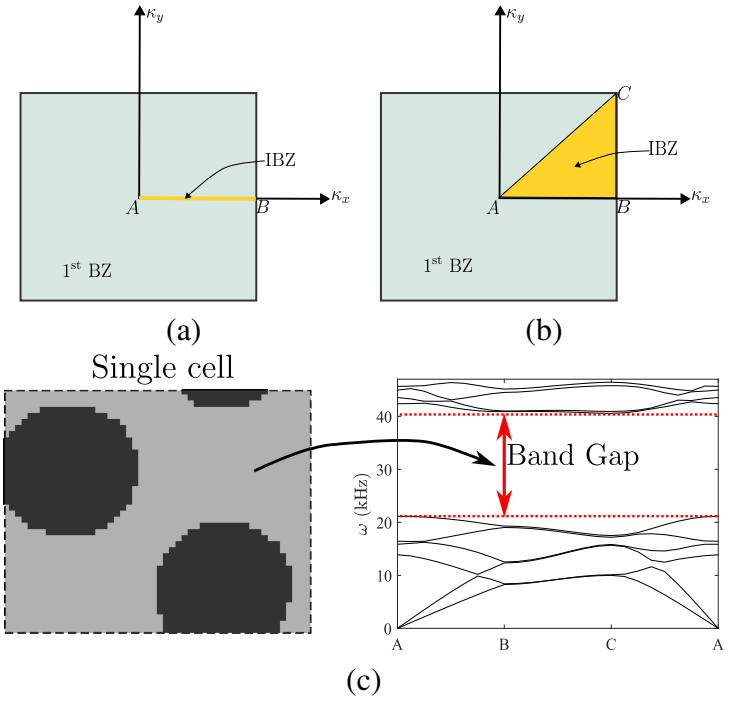

Figure 5: First Brillouin Zone (BZ) and Irreducible Brillouin Zone (IBZ) for square unit cells: (a) 1D-CR lattices; (b) 2D-CR lattices. (c) Representative dispersion diagram along the IBZ boundary, highlighting a band gap between approximately 20 kHz and 40 kHz.

which is particularly convenient for sensitivity analysis.

The dispersion relation of the lattice is obtained by solving Eq. (22) for different values of the wave vector $\boldsymbol{\kappa}$. Owing to symmetry and periodicity considerations, the resulting frequency branches $\omega_j(\boldsymbol{\kappa})$ are typically evaluated over the Irreducible Brillouin Zone (IBZ). For 1D-CR lattices, the IBZ corresponds to $\kappa_x \in [0, \pi/\ell]$, with $\ell = \ell_x$. For isotropic 2D-CR lattices with square unit cells ($\ell_x = \ell_y = \ell$), the IBZ is the triangular region with vertices $A = (0,0)$, $B = (\pi/\ell, 0)$ (or $(0, \pi/\ell)$), and $C = (\pi/\ell, \pi/\ell)$. Dispersion curves are then obtained by tracing the frequency branches along the edges of this triangle (see Figure 5).

Analysis of the dispersion curves enables the identification of band gaps, defined as frequency intervals in which wave propagation is inhibited regardless of the wave vector. Furthermore, substitution of the eigenvalues into Eq. (22) yields the reduced eigenmodes $\widetilde{\boldsymbol{u}}$, which can be mapped back to the full displacement field $\boldsymbol{u}$ on the unit cell using the transformation in Eq. (19).

2.4 Objective function and sensitivity analysis

In this work, the goal is to optimize the unit cell Ω_L of a periodic lattice structure Ω so as to maximize the separation of dispersion branches around a prescribed target fre-

quency (see Figure 5(c)). This task amounts to identifying the material layout within the unit cell that promotes the formation of a band gap centered at the target angular frequency.

Previous studies by Lopes et al. [4, 5] addressed band-gap maximization in beam-like lattices by defining an objective function based on the distance between a user-selected target frequency and the first n_f natural frequencies. In that formulation, higher weights are assigned to frequencies closer to the target frequency ω_0 in order to prioritize their contribution during the optimization.

Despite its effectiveness, this strategy exhibits several limitations. First, the computational burden increases rapidly with n_f, which becomes particularly demanding when the target frequency lies far above the fundamental mode, requiring a large number of eigenfrequencies. Second, the method demands careful tuning prior to execution, as it is necessary to ensure that approximately half of the selected frequencies lie above the target frequency. Third, when the contrast between the material properties is significant, the number of eigenfrequencies located above and below ω_0 may change substantially throughout the optimization. Since n_f is fixed in advance, this situation may lead to numerical instabilities or even failure of the optimization process.

In addition, many existing approaches prescribe the volume fractions of the constituent materials a priori, thereby neglecting alternative distributions that could potentially yield wider band gaps around the target frequency. It is also worth noting that Lopes et al. [5] enforce periodicity conditions over the full lattice, implying that all unit cells must be included in the analysis. This choice considerably increases the computational cost. A significant reduction can be achieved by incorporating Bloch's theorem, as recently demonstrated by other authors (see, e.g., [6]).

To overcome these issues, we propose an optimization framework built upon three main components. The ***first component*** consists in selecting the n_c natural frequencies that are closest to the target frequency. By restricting attention to this subset, the computational cost is reduced, particularly for problems involving high target frequencies. At the same time, the robustness of the procedure is enhanced, since the selected frequencies evolve with the material distribution and consistently bracket the target frequency during the optimization.

The ***second component*** incorporates Bloch's theorem directly into the optimization procedure. As a result, the eigenvalue problem in Eq. (22) is solved only on the unit cell Ω_L, leading to a substantial reduction in computational effort. The dispersion analysis is carried out by solving the eigenvalue problem for multiple wave vectors $\boldsymbol{\kappa}$ along the irreducible Brillouin zone (IBZ) for 1D-CR problems, or along the edges of the IBZ for 2D-CR problems. Accordingly, the following objective function is introduced to promote band-gap formation around the target frequency ω_0, and the

optimization problem is formulated as

$$\begin{aligned} \max_{\mathbf{X}} \quad & f_{obj}(\mathbf{X}) = \frac{1}{n_k} \sum_{k=1}^{\mathcal{K}} f_k(\boldsymbol{\kappa}_k, \mathbf{X}), \\ & f_k(\boldsymbol{\kappa}_k, \mathbf{X}) = \left[\sum_{j=1}^{n_c} \frac{1}{\left(\omega_j(\boldsymbol{\kappa}_k, \mathbf{X})^2 - \omega_0^2\right)^2} \right]^{-1/2}. \end{aligned} \tag{24}$$

Here, $\boldsymbol{\kappa}_k$, $k = 1, \ldots, \mathcal{K}$, denotes the wave vectors sampled along the IBZ contour (see Figure 5), while $\mathbf{X}$ is the design vector describing the material assignment of each finite element. Moreover, $\omega_j(\boldsymbol{\kappa}_k, \mathbf{X})$ is the jth eigenfrequency obtained from the Bloch eigenvalue problem posed on the unit cell Ω_L, as defined in Eq. (22).

Based on numerical experimentation, we observed that selecting $n_k = 25$ wave vectors provides reliable results for both 1D-CR and 2D-CR lattice configurations. The use of a fixed number n_c of eigenfrequencies allows the analysis to focus on the modes that are most relevant to band-gap formation, namely those located closest to ω_0. These modes may change their relative ordering during the optimization, yet they consistently surround the target frequency. Furthermore, squaring the frequency differences promotes symmetric widening of the band gap on both sides of ω_0, while the inverse weighting enhances the contribution of modes located nearest to the target frequency.

The ***third component*** concerns the treatment of material volume fractions. In contrast to conventional approaches, where volume fractions are prescribed in advance, the present methodology does not impose this constraint a priori. Instead, the optimization seeks not only the optimal topology but also the material distribution that yields an optimal volume fraction of material 1, subject to the condition $\tilde{V} - \tilde{V}_{opt} = 0$. This concept is discussed in more detail in Section 3.3. The volume fraction of material 1 is defined as

$$\tilde{V} = \sum_{i=1}^{N} \frac{V_i x_i}{V_{tot}}, \qquad x_i = 1 \text{ or } 0, \tag{25}$$

where V_i denotes the volume of the ith finite element, V_{tot} is the total domain volume, and N is the number of elements in the mesh. The complementary fraction $1 - \tilde{V}$ corresponds to material 2.

Since the optimization is carried out through an evolutionary scheme, a suitable ascent direction must be identified. In this study, this is achieved by means of a gradient-based sensitivity analysis. The sensitivity α_i of the objective function f_{obj} with respect to the design variable x_i is obtained by differentiating Eq. (24), yielding

$$\begin{aligned} \alpha_i &= \frac{1}{n_k} \sum_{k=1}^{n_k} \alpha_{i,k}, \\ \alpha_{i,k} &= \frac{\partial f_k(\boldsymbol{\kappa}_k, \mathbf{X})}{\partial x_i} = \left[\sum_{j=1}^{n_c} \frac{1}{\left(\omega_j^2 - \omega_0^2\right)^2} \right]^{-3/2} \sum_{j=1}^{n_c} \frac{1}{\left(\omega_j^2 - \omega_0^2\right)^3} \frac{\partial \omega_j^2}{\partial x_i}. \end{aligned} \tag{26}$$

Recalling Eq. (23), the derivative of the squared eigenfrequency can be written as

$$\frac{\partial \omega_j^2}{\partial x_i} = \mathbf{u}_j^T \left(\frac{\partial \mathbf{K}}{\partial x_i} - \omega_j^2 \frac{\partial \mathbf{M}}{\partial x_i} \right) \mathbf{u}_j, \tag{27}$$

where the eigenvectors $\mathbf{u}_j$ are assumed to be normalized with respect to the mass matrix $\mathbf{M}$. The derivatives of the stiffness and mass matrices depend on the interpolation of the material properties within element i.

2.5 Material interpolation scheme

The stiffness and mass matrices are computed from interpolated Young's modulus and density fields, respectively, both expressed as continuous functions of the design variables x_i. The dependence of the mass matrix on ρ follows from the discretization of the right-hand side of Eq. (14), whereas the stiffness matrix arises from the left-hand side and depends on the Young's modulus E through Eqs. (3), assuming a fixed Poisson's ratio.

For bi-material problems, a linear rule of mixtures is adopted for both density and Young's modulus, as also considered by Huang and Xie [10]. The resulting interpolation scheme reads

$$\rho(x_i) = x_i(\rho_1 - \rho_2) + \rho_2, \qquad E(x_i) = x_i(E_1 - E_2) + E_2, \tag{28}$$

where ρ_1, E_1 and ρ_2, E_2 denote the density and Young's modulus of materials 1 and 2, respectively, with $E_1 > E_2$. An element with $x_i = 1$ is entirely composed of material 1, while $x_i = 0$ corresponds to material 2. Consequently, the derivatives of the global mass and stiffness matrices take the form

$$\frac{\partial \mathbf{M}}{\partial x_i} = \left(1 - \frac{\rho_2}{\rho_1}\right) \tilde{\mathbf{M}}_i^1, \qquad \frac{\partial \mathbf{K}}{\partial x_i} = \left(1 - \frac{E_2}{E_1}\right) \tilde{\mathbf{K}}_i^1, \tag{29}$$

where $\tilde{\mathbf{M}}_i^1 = A_i^T \mathbf{M}_i^1 A_i$ and $\tilde{\mathbf{K}}_i^1 = A_i^T \mathbf{K}_i^1 A_i$, with A_i denoting the connectivity matrix, and $\mathbf{M}_i^1$ and $\mathbf{K}_i^1$ the elemental mass and stiffness matrices corresponding to material 1.

3 Numerical implementation. BESO procedure

In this work, the Bi-directional Evolutionary Structural Optimization (BESO) method is employed, which allows materials to be removed and added simultaneously. This topology optimisation method is based on identifying a design that maximises the desired criterion through successive alterations of the topology. In this process, each element is assigned a design variable x_i, where $x_i = 1$ indicates the presence of material 1, and $x_i = 0$ indicates the presence of material 2.

3.1 Algorithm

The BESO method is implemented here following a strategy closely aligned with that proposed in [9]. BESO is a well-established topology optimization algorithm, widely adopted due to its conceptual simplicity and numerical robustness. As a gradient-based method, it relies on a sensitivity analysis derived from the partial derivative of the objective function, as defined in Eq. (26) and Eqs. (29).

Since BESO operates within a discrete design framework, the design variables assume only binary values, such that the ith finite element is assigned either material 1 ($x_i = 1$) or material 2 ($x_i = 0$). At each iteration, the values of these design variables are updated based on a sensitivity analysis that quantifies the contribution of each element to the objective function.

The optimization procedure is initialized with all elements in the design domain assigned to material 1. During subsequent iterations, elements are progressively converted to material 2 until the condition $\tilde{V} - \tilde{V}_{opt} = 0$ is satisfied, where $\tilde{V}_{opt}$ represents the optimal volume fraction identified as an output of the optimization process proposed in this work. A schematic description of the adopted BESO procedure is provided in Figure 6.

The parameters specified under the "Input" block in Figure 6 must be prescribed by the user. The parameter ER denotes the *evolution rate* and controls the percentage of material 1 removed at each iteration, while AR_{max} represents the *maximum addition rate*, defining the maximum percentage of material 2 that may be converted back to material 1.

Although increasing the values of ER and AR_{max} generally reduces the total number of iterations, excessively large values may compromise the stability of the optimization process. Consequently, these parameters must be selected with care in order to ensure a smooth and reliable evolution of the topology. As discussed in Section 2.4, the target volume fraction $\tilde{V}_{opt}$ is not prescribed as an input parameter in the present formulation, but is instead obtained as an outcome of the optimization procedure, as detailed in Section 3.3.

3.2 Numerical filter

The numerical filtering strategy adopted in this work follows the approach introduced by Huang and Xie [8]. The filter plays a crucial role in suppressing checkerboard patterns and reducing mesh dependency in the optimized topology. Its implementation requires the specification of the parameter r_{min}, commonly interpreted as the minimum admissible feature size of the design.

The filtering process consists of two consecutive operations applied to the elemental sensitivities. First, the sensitivity α_i associated with each element is distributed to its surrounding nodes. Subsequently, the nodal sensitivities are averaged to compute the filtered elemental sensitivities. The nodal sensitivity β_j associated with the jth

Algorithm 1: BESO procedure

Input : Define optimization parameters: n_c, n_k, n_s, n_e, ER, AR_{max}, r_{min}, τ

Define design domain, boundary conditions (Bloch Theorem) and finite element mesh

Calculate eigenvalues and identify eigenvectors

Start iteration counter: $loop = 0$

Start volume fraction of material 1: $\tilde{V} = 1$

Start optimal volume fraction: $\tilde{V}_{opt} = 0$

while $\tilde{V}^{(loop)} \neq \tilde{V}_{opt}$ **or** $error < \tau$ **do**

- $loop = loop + 1$
- Evaluate sensitivities $\alpha_i^{(loop)}$ (Section 2.2)
- Filter sensitivity numbers (Section 3.2)
- Calculate next targeted volume
- Update topology $x_i^{(loop)}$
- Calculate eigenvalues and eigenvectors
- Evaluate objective function
- **When** $loop > n_s$**:** $\tilde{V}_{opt}$ detected? (Section 3.3) $\begin{cases} \text{if } no, & \tilde{V}_{opt} = 0 \\ \text{if } yes, & \tilde{V}^{loop} = \tilde{V}_{opt} \end{cases}$
- Update volume $\tilde{V}^{(loop)}$
- Calculate $error$

Output: Optimized topology $x_i^{(loop)}$ and optimal volume fraction $\tilde{V}_{opt}$

Figure 6: Flowchart of the BESO topology optimization procedure adopted in this work.

node is computed as

$$\beta_j = \sum_{i=1}^{m} w_i \alpha_i, \tag{30}$$

where m denotes the number of elements sharing the jth node and w_i is a weighting factor defined by

$$w_i = \begin{cases} \dfrac{1}{m-1}\left(1 - \dfrac{r_{ij}}{\sum_{i=1}^{m} r_{ij}}\right), & \text{if } m > 1, \\ 1, & \text{if } m = 0, \end{cases} \tag{31}$$

with r_{ij} denoting the distance between the centroid of the ith element and the jth node.

The filtered sensitivity of the ith element is then obtained as

$$\tilde{\alpha}_i = \frac{\sum_{j=1}^{n_d} \tilde{w}(r_{ij})\beta_j}{\sum_{j=1}^{n_d} \tilde{w}(r_{ij})}, \qquad \tilde{w}(r_{ij}) = r_{min} - r_{ij}, \tag{32}$$

where n_d is the number of nodes satisfying $r_{ij} < r_{min}$. Once the filtered sensitivities are obtained, the topology is updated by assigning $x_i = 1$ to the elements with the highest sensitivity values, while the remaining elements are assigned $x_i = 0$, following the procedure described in [9].

3.3 Determination of optimal volume fraction

In most BESO-based topology optimization studies, the final volume fraction of material 1 is prescribed by the user. Under this conventional approach, the maximization of the objective function f_{obj} depends solely on the spatial distribution of a fixed amount of material within the design domain, which typically necessitates multiple optimization runs to identify the volume fraction yielding the highest objective value.

In the present work, a modified BESO algorithm is proposed in which the volume fraction is treated as an output variable of the optimization process. The algorithm therefore identifies not only the optimal topology, but also the optimal volume fraction $\tilde{V}_{opt}$ that maximizes f_{obj}, which is subsequently adopted as the final volume fraction of material 1.

The proposed procedure is described below and illustrated by the schematic example shown in Figure 7, where the evolution of both f_{obj} and the volume fraction over the optimization iterations is displayed.

4 Numerical examples

In this section, an optimization case is going to be studied for lattice structures formed by the periodic repetition of a unit cell in 1D (1D-CR). In this case, the properties of

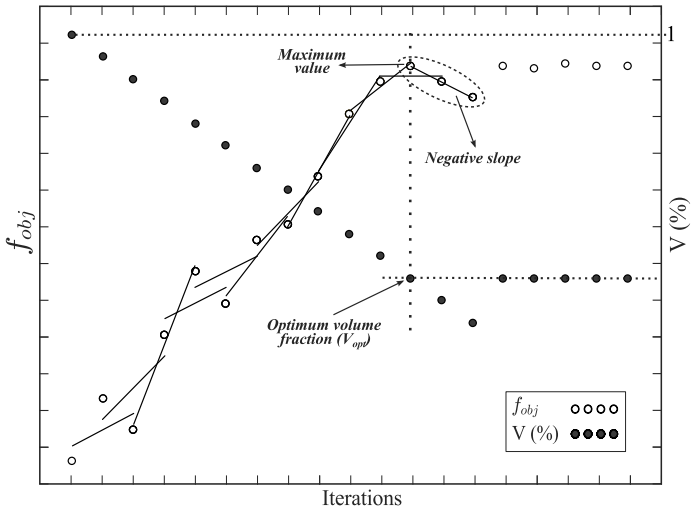

Figure 7: Illustrative example of the procedure used to identify $\tilde{V}_{opt}$, shown for $n_s = 3$.

both materials are $E_1 = 210$ GPa; $\rho_1 = 7800$ kg/m^3 and $E_2 = 21$ GPa; $\rho_2 = 780$ kg/m^3.

We consider a lattice structure that seeks to filter a target frequency of $\omega_0 = 17$ kHz, this being formed by a unit cell of 0.125×0.1 m^2, which is discretized as 50×40 identical quadrilateral finite elements with two degrees of freedom per node (displacements in x and y directions). The adopted BESO input parameters are: $n_c = 10$, $n_k = 25$, $n_e = 5$, $ER = 2$ %, $AR_{max} = 2$ %, $r_{min} = 10$ mm and $\tau = 10^{-6}$. Figure 8 (c) displays the evolution of both f_{obj} and volume fraction during the optimization process, which founds that $\tilde{V}_{opt} = 0.48$ after 30 iterations, then keeping this value until satisfying the stopping criterion after 10 additional iterations, reaching a unit cell with the topology shown in Figure 8 (a), where material 1 is colored in black and material 2 in grey. Note that the dispersion relation of a lattice structure formed by this unit cell, presented in Figure 8 (b), shows a wide Band Gap around the target frequency $\omega_0 = 17$ kHz (dots line), specifically from 9.54 kHz to 26.37 kHz. These results are in agreement with those presented in [5], where a beam formed by 8 unit cells is studied, considering a volume fraction of material 1 of 0.5, which is an input set by the authors. Note that each of the 8 cells that compose the optimized beam presents a topology very similar to the one in Figure 8 (a), featuring a separation between natural frequencies that match the Band Gap appearing in Figure 8 (b).

5 Conclusions

In this work, a novel BESO-based topology optimization procedure has been proposed for the design of lattice structures with target dynamic properties. Unlike conventional BESO implementations, the method treats the volume fraction of material 1 as an output variable, allowing the simultaneous determination of both the optimal topology

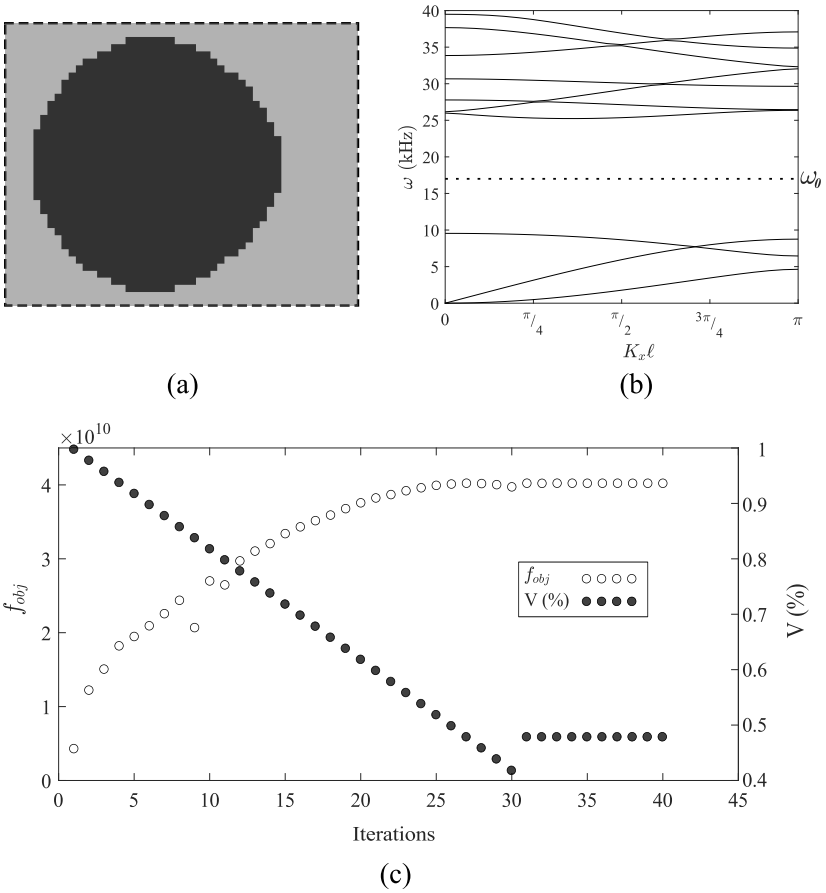

Figure 8: Results from the topological optimisation of a unit cell of 0.125×0.1 m^2, considering a target frequency $\omega_0 = 17$ kHz, and $n_c = 10$, $n_k = 25$, $n_e = 5$, $ER = 2$ %, $AR_{max} = 2$ %, $r_{min} = 10$ mm and $\tau = 10^{-6}$. (a) Topology design (material 1 colored in black and material 2 in grey). (b) Dispersion relation. (c) Evolution of f_{obj} and volume fraction.

and the optimal material fraction that maximizes the objective function. A slope-based detection strategy was introduced to identify the optimal fraction during the iterative evolution, while a historical average-based stopping criterion ensured reliable convergence of the topology. Numerical filtering was employed to avoid checkerboard patterns and mesh dependency, guaranteeing smooth and physically meaningful designs. The methodology was successfully applied to both one-dimensional and two-dimensional periodic lattices, demonstrating the formation of wide band gaps around target frequencies and reproducing the results of previously reported studies with reduced computational cost.

The numerical examples confirm that the proposed procedure is robust, efficient, and capable of automatically adjusting the material distribution and fraction to achieve optimal performance. By combining sensitivity-based material updating, volume fraction optimization, and convergence control, the method provides a systematic and generalizable framework for the design of frequency-targeted lattice structures. This approach can be readily extended to more complex unit cells, multi-material configurations, and higher-dimensional lattices, paving the way for advanced metamaterial designs and other applications where precise control of dynamic behavior is required.

6 Acknowledgements

F. Gómez-Silva acknowledges support from MCIN/AEI/10.13039/501100011033 and from FEDER, UE under Grant number PID2021-123294OB-100. This work has been also supported by the Madrid Government (Comunidad de Madrid-Spain) under the Multiannual Agreement with UC3M in the line of Excellence of University Professors (EPUC3M24), and in the context of the V PRICIT (Regional Programme of Research and Technological Innovation). R. Ortigosa and J. Martínez-Frutos acknowledge the support of grant PID2022-141957OA-C22 funded by MICIU/AEI/10.13039/501100011033 and by "ERDF A way of making Europe".

References

[1] F. Bloch, "Über die quantenmechanik der elektronen in kristallgittern", Zeitschrift für Physik, 52, 555–600, 1929.

[2] F. Gómez-Silva, R. Zaera, "Novel low-order continuum models for the dynamic behaviour of microstructured plates based on a beam-grid lattice", Thin-Walled Structures, 191, 111084, 2023.

[3] F. Gómez-Silva, R. Zaera, "Low-order continualization of an anisotropic membrane lattice with next-nearest interactions. Enhanced prediction of its dynamic behaviour", European Journal of Mechanics – A/Solids, 97, 104801, 2023.

[4] H.N. Lopes, D.C. Cunha, R. Pavanello, J. Mahfoud, "Numerical and experimental investigation on topology optimization of an elongated dynamic system", Mechanical Systems and Signal Processing, 165, 108356, 2022.

[5] H.N. Lopes, J. Mahfoud, R. Pavanello, “High natural frequency gap topology optimization of bi-material elastic structures and band gap analysis”, Structural and Multidisciplinary Optimization, 63, 2325–2340, 2021.

[6] A. Dalklint, M. Wallin, K. Bertoldi, D. Tortorelli, “Tunable phononic bandgap materials designed via topology optimization”, Journal of the Mechanics and Physics of Solids, 163, 104849, 2022.

[7] X. Huang, Z.H. Zuo, Y.M. Xie, “Evolutionary topological optimization of vibrating continuum structures for natural frequencies”, Computers & Structures, 88, 357–364, 2010.

[8] X. Huang, Y.M. Xie, “Convergent and mesh-independent solutions for the bi-directional evolutionary structural optimization method”, Finite Elements in Analysis and Design, 43, 1039–1049, 2007.

[9] X. Huang, M. Xie, *Evolutionary Topology Optimization of Continuum Structures: Methods and Applications*, John Wiley & Sons, 2010.

[10] X. Huang, Y.M. Xie, “Bi-directional evolutionary topology optimization of continuum structures with one or multiple materials”, Computational Mechanics, 43, 393–401, 2009.